CONDENSED MATTER PHYSICS

Imaging quantum spin Hall edges in monolayer WTe_2

Yanmeng Shi[1]*, Joshua Kahn[2]*, Ben Niu[1,3]*, Zaiyao Fei[2], Bosong Sun[2], Xinghan Cai[2], Brian A. Francisco[1], Di Wu[3], Zhi-Xun Shen[4], Xiaodong Xu[2†], David H. Cobden[2†], Yong-Tao Cui[1†]

A two-dimensional (2D) topological insulator exhibits the quantum spin Hall (QSH) effect, in which topologically protected conducting channels exist at the sample edges. Experimental signatures of the QSH effect have recently been reported in an atomically thin material, monolayer WTe_2. Here, we directly image the local conductivity of monolayer WTe_2 using microwave impedance microscopy, establishing beyond doubt that conduction is indeed strongly localized to the physical edges at temperatures up to 77 K and above. The edge conductivity shows no gap as a function of gate voltage, and is suppressed by magnetic field as expected. We observe additional conducting features which can be explained by edge states following boundaries between topologically trivial and nontrivial regions. These observations will be critical for interpreting and improving the properties of devices incorporating WTe_2. Meanwhile, they reveal the robustness of the QSH channels and the potential to engineer them in the monolayer material platform.

INTRODUCTION

In a two-dimensional (2D) topological insulator (TI), gapless states are guaranteed to exist at the edges separating the topologically nontrivial bulk from the topologically trivial surroundings (*1*–*6*). When the chemical potential lies in the bulk energy gap, charge transport can occur only through these edge states. Because the edge states are helical (the electron spin is locked to its momentum), elastic backscattering is suppressed because of time reversal symmetry, and under ideal circumstances, this gives ballistic electron transport and consequently a quantized conductance, suppressed by magnetic field, which is considered the hallmark of the quantum spin Hall (QSH) effect (*7*).

Signatures of the QSH effect have been reported in HgTe/CdHgTe quantum wells (*8*–*11*) and InAs/GaSb double quantum wells (*12*–*15*) and, more recently, in monolayers of the layered semimetal WTe_2 (*16*–*19*). These experiments, however, presented some puzzles. Although edge conduction was seen in all these systems, the measured conductance often showed large deviations from the expected quantized value (*8*–*10*, *12*, *13*, *15*). In addition, a combination of transport and scanning probe microscopy studies on the quantum well systems revealed that topologically trivial conduction could also occur at the edges and that the magnetic field dependence was surprisingly small (*20*–*22*). It should thus be revealing to examine this new monolayer system in the same way. Here, we apply microwave impedance microscopy (MIM) (*22*–*25*) to monolayer WTe_2 devices, directly mapping the local conductivity. We observe gapless conduction localized to the sample edges, whose electrical and geometrical behavior is consistent with the QSH effect. In addition, MIM reveals other important aspects of the conduction properties of this system that could not be deduced from transport, providing crucial insights for optimizing devices and opportunities to access and manipulate the helical edge channels.

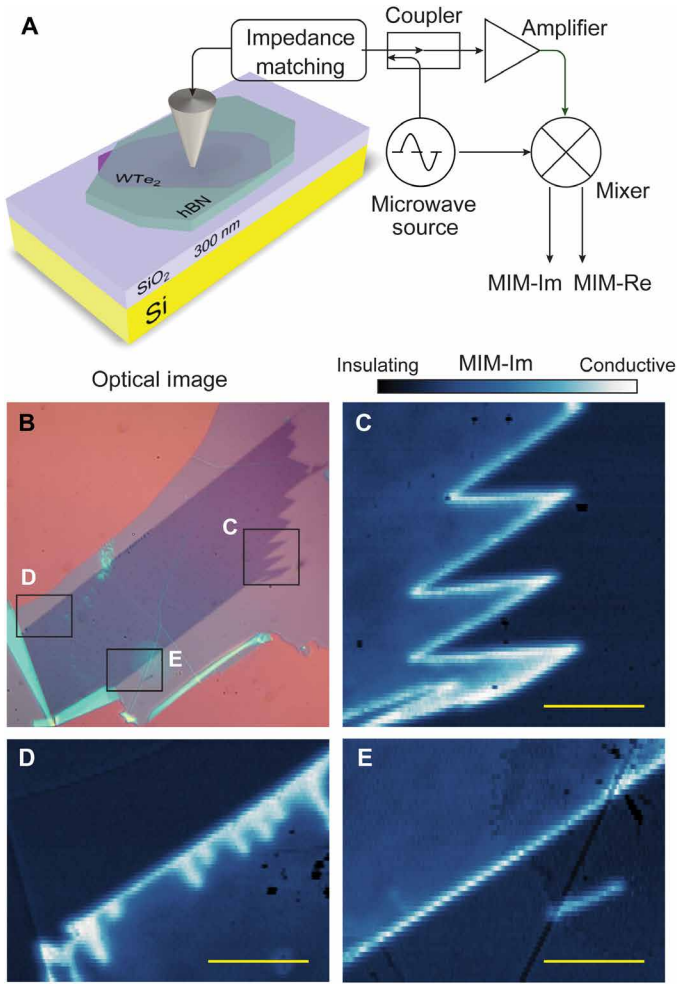

Fig. 1. Imaging edge conductivity in monolayer WTe_2. (**A**) Schematics of the technique and device structure. (**B**) Optical image of a WTe_2 monolayer exfoliated onto SiO_2 and covered with a 10-nm-thick hBN. (**C** to **E**) MIM-Im images of the regions marked in (B), measured at $T = 8$ K and $B = 0$. Scale bars, 5 μm.

[1]Department of Physics and Astronomy, University of California, Riverside, CA 92521, USA. [2]Department of Physics, University of Washington, Seattle, WA 98195, USA. [3]National Laboratory of Solid State Microstructures, Department of Materials Science and Engineering, College of Engineering and Applied Sciences, and Collaborative Innovation Center of Advanced Microstructures, Nanjing University, Nanjing 210093, China. [4]Geballe Laboratory for Advanced Materials, Stanford University, Stanford, CA 94305, USA.
*These authors contributed equally to this work.
†Corresponding author. Email: xuxd@uw.edu (X.X.); cobden@uw.edu (D.H.C.); yongtao.cui@ucr.edu (Y.-T.C.)

RESULTS

MIM measurement of edge conduction in monolayer WTe_2

The MIM technique probes the local conductivity by analyzing the imaginary and real parts of the complex admittance, which we call MIM-Im and MIM-Re, respectively, between a sharp conducting tip and the sample (Fig. 1A). MIM-Im characterizes the amount of screening of the microwave electric field at the tip by the sample, while MIM-Re characterizes the dissipation generated by the induced oscillating currents in the sample. The responses of MIM-Im and MIM-Re to changing local resistivity can be obtained via finite element analysis (an example is plotted in Fig. 2E): MIM-Im increases monotonically as the resistivity decreases, while MIM-Re is strongly peaked at an intermediate resistivity value. These response curves serve as guides for interpreting the MIM measurements.

We first demonstrate the edge conduction in a simple sample structure: a monolayer WTe_2 flake exfoliated onto SiO_2 and directly covered with a larger flake of hexagonal boron nitride (hBN) (see Materials and Methods for fabrication details and table S1 for information on all samples). Figure 1B shows an optical image, and Fig. 1 (C to E) show MIM-Im measurements of selected regions as marked in Fig. 1B, taken at temperature $T = 8$ K and magnetic field $B = 0$. The MIM-Im signal in the interior of the flake is comparable to that over the substrate, indicating a highly insulating state. Meanwhile, a bright narrow line indicating much higher conductivity follows the entire outline of the flake, whether it is straight (Fig. 1E) or sharply zigzagged (Fig. 1C). Moreover, in Fig. 1D, we see a series of short bright lines intruding into the interior that do not correspond to features that are visible optically. These are almost certainly due to small tears that are narrow enough that the two opposing edges of each tear cannot be resolved; thus, they appear as single lines, albeit thicker and brighter than the line following the outer edge. These observations unambiguously confirm the existence of edge conduction in monolayer WTe_2. Furthermore, the strict conformity with the microscopic edge geometry agrees with the topological nature of helical edge channels (see section S2 for more images of this sample).

Gate and magnetic field dependence of the edge conduction

In a 2D TI, the helical edge state dispersion spans the bulk gap, connecting the conduction and valence bands, so the edge conduction should persist while the bulk chemical potential is tuned across the gap (*7*, *26*). This property is in contrast with edge conduction due to in-gap states or to band bending in a trivial insulator, which exists only over a limited energy range (*27*–*29*). To study this behavior, we turn to samples with electrical contacts that allow simultaneous MIM and transport measurements while also applying a gate voltage V_g to the silicon substrate (see section S3). Figure 2 presents results from

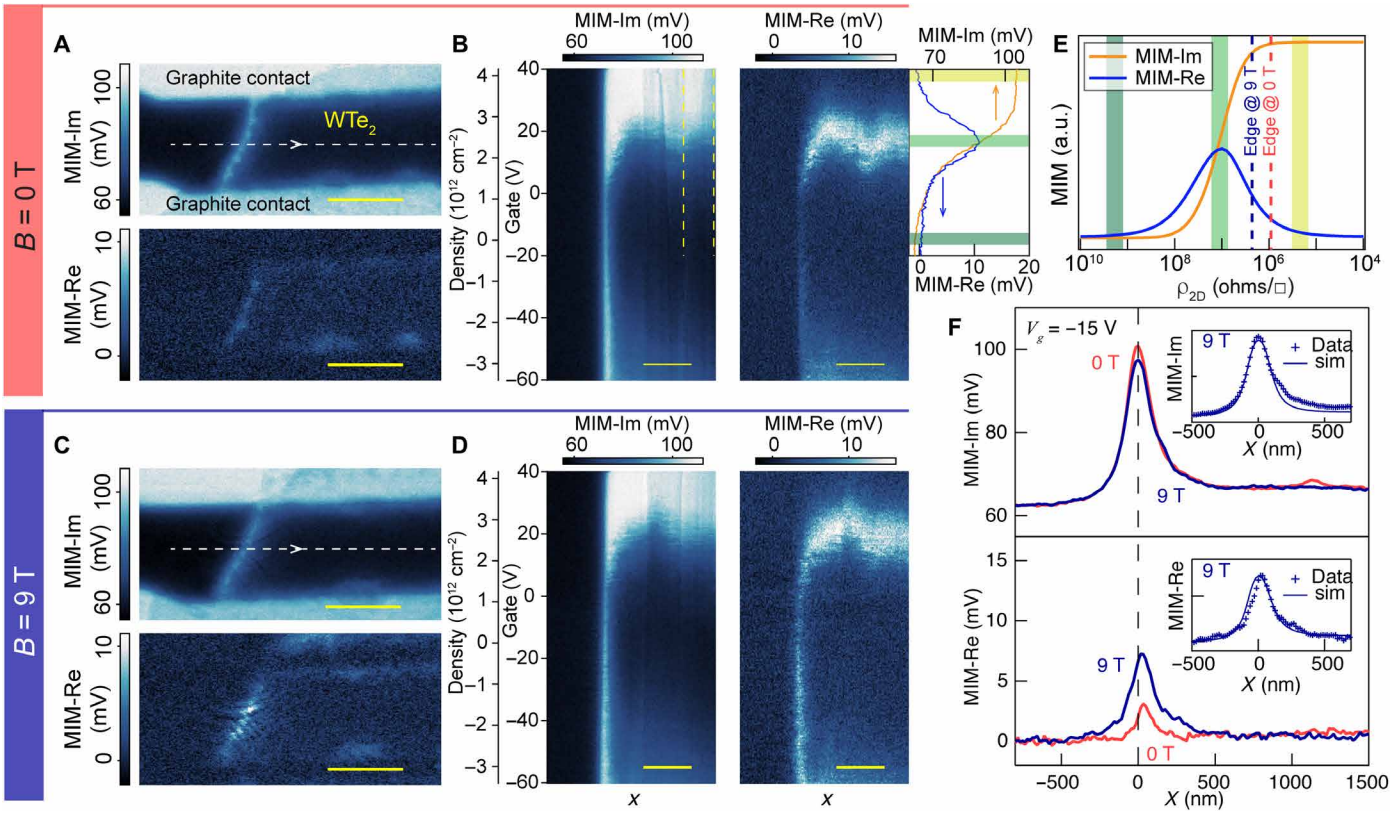

Fig. 2. Gate and magnetic field dependence of the edge conduction. (**A**) MIM-Im and MIM-Re images of part of a monolayer WTe_2 flake between two thin graphite contacts, measured at $B = 0$. (**B**) MIM-Im and MIM-Re obtained along the dashed line in (A) and stacked as a function of gate voltage. The corresponding carrier density is plotted on a separate axis, which includes an offset by the charge neutrality point. The upper right panel plots the averaged linecuts over the bulk region indicated by the two dashed lines in the MIM-Im channel, from $V_g = -20$ to 40 V. (**C** and **D**) Real-space images and gate voltage dependence at $B = 9$ T. (**E**) MIM-Im and MIM-Re signals as a function of 2D resistivity. The colored bands match those in the linecuts in (B), and the dashed lines indicate the 2D resistivity at the edge for $B = 0$ and 9 T, estimated from the line traces in (F). a.u., arbitrary units. (**F**) Averaged MIM-Im (top) and MIM-Re (bottom) traces of linecuts in between the two contacts with the edge position aligned at both $B = 0$ and 9 T. Insets are the comparison between the 9 T line traces and the simulated MIM responses. The measurement temperature is 5 K. Scale bars, 1 μm.

a monolayer WTe_2 device incorporating two thin graphite contacts separated by ~1.2 μm. Figure 2A shows MIM-Im and MIM-Re images at $B = 0$ and $V_g = -15$ V, which we identify as the charge neutrality point (CNP) in the bulk through gate voltage dependence measurement presented below. Again, the small MIM signals in the interior of the flake signify a highly insulating state, while the large MIM-Im signal near the WTe_2 edge indicates a highly conductive state.

To probe the gate voltage dependence of both the edge and bulk conductivity, the tip is scanned repeatedly along a single line crossing the WTe_2 edge halfway between the contacts as V_g is varied from −60 to +40 V (Fig. 2B). Over this range, the bulk goes from mildly conducting p-doped through insulating to highly conducting n-doped, implying that the chemical potential is tuned across the bulk gap. All the while, the edge remains highly conductive, just as expected for a topological edge mode, whereas a trivial edge conduction mode should have a stronger gate dependence and is expected to disappear in a certain range of gate voltages due to depletion (*29*). Near the CNP, since both MIM-Im and MIM-Re in the bulk are small, the conductivity value falls on the highly insulating side of the response curve (Fig. 2E). Upon gating to either the n- or p-doped side, the bulk conductivity increases; thus, MIM-Im should increase monotonically while MIM-Re should exhibit a peak. The measured bulk signals show exactly this behavior (see the annotations in Fig. 2, B and E), albeit with an asymmetry suggesting different carrier mobilities on the p-doped and n-doped sides.

In a magnetic field, the helical edge states are expected to mix, opening a Zeeman gap and suppressing conduction when the chemical potential at the edge is near this gap (*26*). In previous dc transport measurements, the edge conduction was indeed suppressed, although with a complicated dependence on gate voltage probably due to disorder effects (*16*, *19*). Figure 2C shows MIM images similar to those in Fig. 2A but taken in a perpendicular field $B = 9$ T. Edge conduction can still be clearly resolved. There is a visible increase in MIM-Re when the field is applied, which occurs consistently over a wide range of doping levels as seen in the gate dependence in Fig. 2D. On the other hand, the MIM signals in the bulk are little changed; hence, the effect of the magnetic field is almost entirely at the edges, consistent with transport measurements (*16*, *19*). This also implies that the material has a low carrier mobility, so that Landau levels do not form and there is no quantum Hall effect, in contrast with the situation in semiconductor quantum wells (*8*). To study the effect on the edge signals more quantitatively, we plot in Fig. 2F MIM traces taken across the edge at 0 and 9 T on the same axes. To improve signal-to-noise ratios, these traces are obtained by averaging horizontal linecuts in the MIM images taken near the CNP with the edge position aligned. We see that, when 9 T is applied, MIM-Im decreases while MIM-Re increases. Referring to the MIM response curves, these changes indicate an increase in the edge resistivity (see the dashed lines in Fig. 2E) that is qualitatively consistent with the dc transport results (*16*, *19*) (see section S4 for the simulation and a discussion quantitatively comparing MIM and transport results in a magnetic field).

Additional conduction features observed inside monolayer WTe_2

In addition to the physical edges, conducting features are frequently observed in the interior of samples, which can be interpreted as topological boundary modes separating regions of different topological characters, as illustrated in Figs. 3 and 4. Figure 3A is an optical image of a monolayer WTe_2 flake on SiO_2 that is mostly covered by an hBN flake, although a corner is exposed and there is also a folded bilayer region. In the MIM-Im image (Fig. 3B), a conducting line is seen all along the exterior monolayer edge where it is under the hBN but not on the edge of the folded bilayer. This observation suggests that the folded bilayer in this sample is topologically trivial, in which case, in principle, an edge state should exist at the boundary between the pristine monolayer and the folded bilayer. However, the portion of the bilayer near the boundary appears to be somewhat degraded, which complicates the observation of edge conduction nearby (see section S5 for more details). On the other hand, at the exposed part, the conducting line clearly runs along the edge of the hBN rather than around the exterior edge. Since the exposed part will be oxidized and thus trivially insulating, this behavior is just as expected given the topological nature of the QSH edge states. In addition, we see conducting lines cutting across the interior of the monolayer under the hBN. These lines are not likely to be folds because they are not visible in topography, as measured by atomic

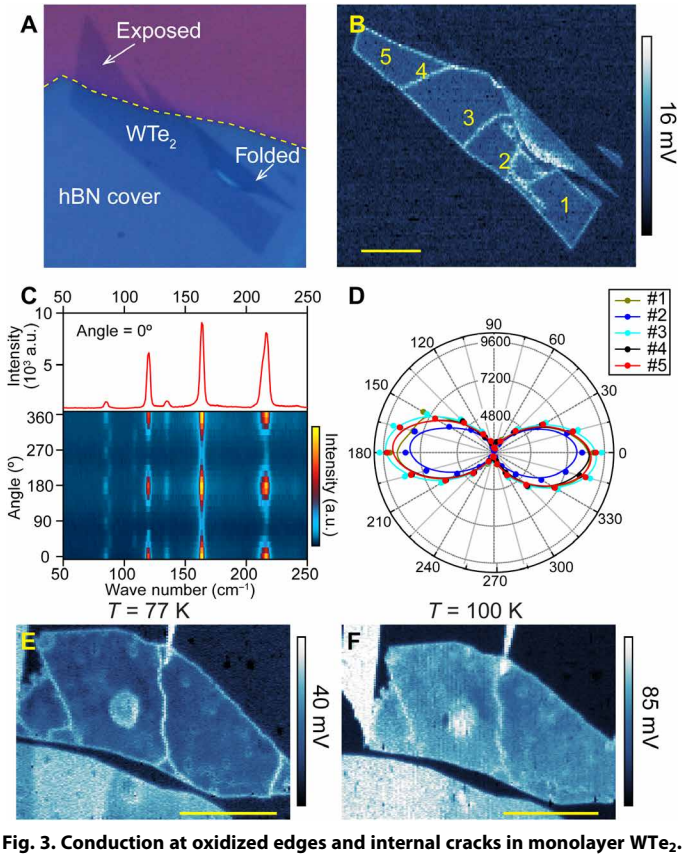

Fig. 3. Conduction at oxidized edges and internal cracks in monolayer WTe_2. (**A**) Optical image of a monolayer WTe_2 flake partially covered by hBN. (**B**) MIM image of the same flake measured at $T = 480$ mK and $B = 0$. High conductivity is observed both at the physical edges and along lines in the interior. (**C**) Polarized Raman spectroscopy and angular dependence measured at 5 K, for spot #5 marked in (B). (**D**) Polar plot of the 163 cm^{-1} Raman peak intensity for the five spots marked in (B). All have the same angular dependence, showing that the crystal axes are the same and implying that the lines are cracks. (**E** and **F**) MIM-Im images of another monolayer WTe_2 sample at 77 K (E) and 100 K (F) (Note that the scanned areas are slightly shifted and include a piece of graphite contact near the upper left corner in the 100 K image.) Scale bars, 5 μm.

force microscopy (AFM; see section S5). We can also rule out grain boundaries using polarized Raman spectroscopy: The 1T′ structure is orthorhombic, so the intensities of all Raman peaks show a two-fold rotationally symmetric dependence on the polarization angle relative to the crystal axes (Fig. 3C). Figure 3D is a polar plot of the Raman intensity at each of the five points labeled in Fig. 3B, showing that the crystal axes are the same everywhere. The only explanation remaining is narrow cracks, generated during either exfoliation of the WTe_2 or transfer of the hBN on top. QSH edge states should follow both edges of a crack, and indeed, the gate dependence of the internal lines is very similar to that of the exterior edges (see section S6). Figure 3 (E and F) shows MIM-Im images of another sample, illustrating that the edge conduction, including that at internal cracks, dominates the conductivity even at 77 K and is still visible up to 100 K, which is again consistent with transport measurements (*16*, *19*).

In Fig. 4, we illustrate some other phenomena revealed by our technique, which have important consequences for device fabrication and performance. Figure 4 (A, C, and E) shows MIM-Im images of regions of three different monolayer WTe_2 devices, each with a pair of encapsulated thin Pt contacts and each showing poor dc electrical characteristics. All exhibit not only conducting lines at the edges but also conductivity elsewhere in various patterns. In Fig. 4A, one can discern a strip of enhanced conductivity in the WTe_2 bulk adjacent to the contact edges, most apparent in the MIM-Re image shown in Fig. 4B. Similar features were seen in other devices, including the one with graphite contacts presented in Fig. 2. On the other hand, in Fig. 4C, a narrow dark strip of very low conductivity surrounds each contact, separated by a bright conducting line from the monolayer bulk. In Fig. 4 (C and E), we see a network of conducting internal lines similar to those in Fig. 3B. In addition, in Fig. 4E, we also see many small conducting rings, which match well the outlines of small blisters (height, 3 to 5 nm) visible in the simultaneous topography scan (Fig. 4F). Two similar but fainter rings are just discernable in Fig. 4A.

DISCUSSION

The cartoon in Fig. 4G illustrates our interpretation of these features. First, there are cracks and tears that the edge modes conform to, as described earlier. Next, the strips around the contacts can be explained by oxidation due to "tenting" of the hBN/WTe_2 over the edges of the contact metal, which permits access by air or liquids. On the basis of the observations in multiple samples, we speculate that weak oxidation increases conductivity and stronger oxidation produces a trivial insulator, leading to an edge mode at its boundary with the unoxidized WTe_2 as seen in Fig. 3B. The blisters in Fig. 4E are probably also a result of chemical damage that turns spots of the WTe_2 into a different insulating material, leaving a ring-shaped edge mode surrounding each internal (topologically trivial) hole in the QSH material. Another possibility that we considered is that strain around the blisters modifies the electronic structure (*6*), but the blisters are much shallower than those typically produced by trapped contamination (*30*) and are unlikely to produce the required ring of high strain.

The presence of such cracks, rings, contact-surrounding strips, and other internal features seen in Figs. 3 and 4 could produce misleading dc transport results. For instance, they could conduct in parallel with the exterior edges, introduce large contact resistances, or block current along edges, depending on details. Their presence is difficult to detect and control during device fabrication. Fortunately, MIM can be performed on transport device structures (before placing a top gate) to probe them. In addition, our results imply

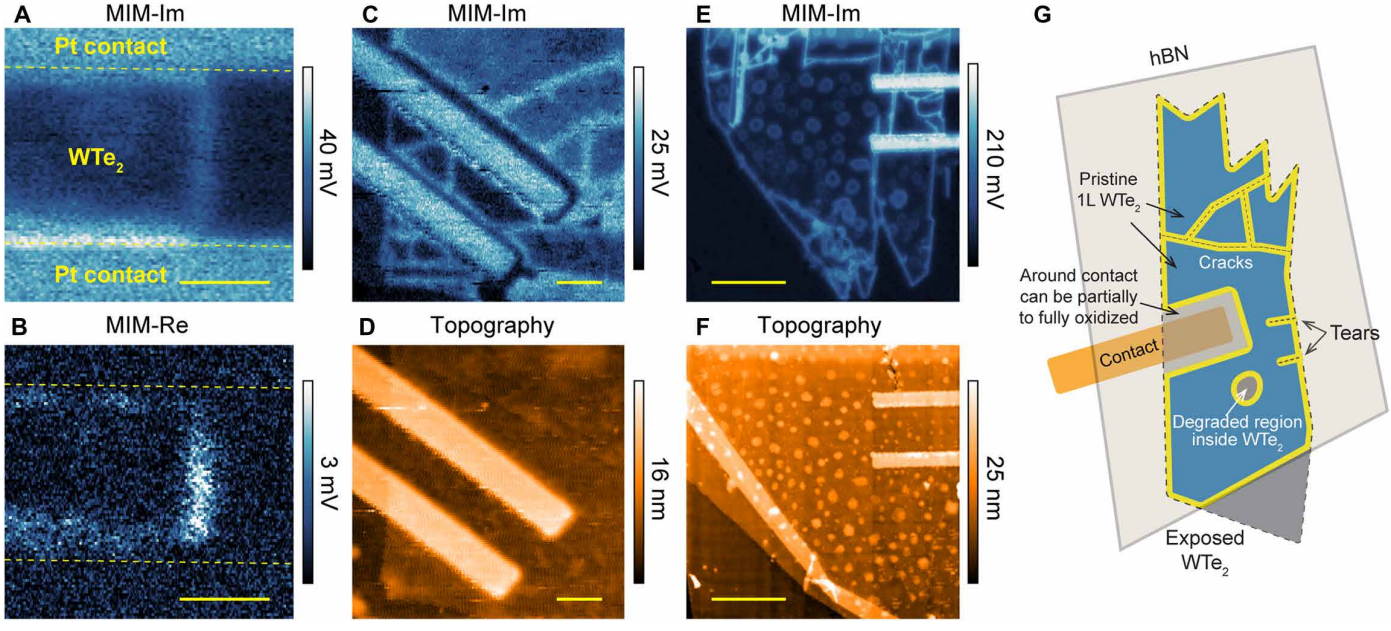

Fig. 4. Conductivity features near contacts and around defects in monolayer WTe_2. (**A** and **B**) MIM-Im and MIM-Re images of part of a monolayer (1L) WTe_2 device between two Pt contacts, measured at $T = 480$ mK, $V_g = 0$ V, and $B = 12$ T. Scale bars, 500 nm. (**C** and **D**) MIM-Im and topography images of part of a second monolayer WTe_2 device, measured at $T = 10$ K, $V_g = 3.3$ V, and $B = 0$ T. In the topography, the flake appears continuous, but MIM reveals that the regions around the contacts are highly insulating (dark). Scale bars, 1 μm. (**E** and **F**) MIM-Im and topography images of part of a third monolayer WTe_2 device, measured at $T = 10$ K, $V_g = 0$ V, and $B = 9$ T. The small rings visible in the MIM-Im image correspond to the blisters in the topography image. Scale bars, 3 μm. (**G**) Cartoon illustrating various conductivity features observed in our experiments.

that, in this monolayer QSH system, edge channels could be created on demand, for various applications, by locally inducing either oxidation or fracture. That could, for example, allow the helical modes on two edges to be brought very close to each other or to other objects such as superconductors, or allow modes to be crossed and tunnel-coupled with each other, which may offer new opportunities for the study and manipulation (*31*) of QSH edge modes. Such configurations represent an advantage of atomically thin materials as they are difficult to achieve in semiconductor heterostructure QSH systems where the edge states are buried and are defined by depletion fields (*8*, *12*).

MATERIALS AND METHODS

Device fabrication

Graphite, hBN, and WTe_2 flakes were prepared by mechanical exfoliation of crystals onto a 285-nm SiO_2 substrate. The graphite and hBN were exfoliated under ambient conditions. The WTe_2 was exfoliated in an inert atmosphere, provided by a nitrogen-filled glove box, to avoid degradation. Suitable flakes were optically identified, and a polymer stamp transfer method (*32*) was used to construct the devices. The simplest devices were made by placing an hBN onto a monolayer of WTe_2. This capping hBN allowed the WTe_2 to be removed from the glove box without oxidation. Devices with contacts also required a bottom layer of hBN to properly encapsulate the WTe_2. The contacts were either exfoliated graphite flakes or evaporated V/Au or Pt metal patterned using standard e-beam lithography and lift-off processes.

MIM measurement

MIM measurements were performed by delivering a small microwave excitation of ~0.1 μW at a fixed frequency in the range 1 to 10 GHz to a chemically etched tungsten tip (*25*). The reflected signal was analyzed to extract the demodulated output channels, MIM-Im and MIM-Re, which were proportional to the imaginary and real parts of the admittance between the tip and the sample, respectively. To enhance the MIM signal quality, the tip was excited to oscillate at a frequency of ~32 kHz with an amplitude of ~8 nm. The resulting oscillation amplitudes of MIM-Im and MIM-Re were then extracted using a lock-in amplifier to yield d(MIM-Im)/dz and d(MIM-Re)/dz, respectively. The d(MIM)/dz signals are free of fluctuating backgrounds, thus enabling more quantitative analysis, while their behavior is very similar to that of the standard MIM signals (*25*). Here, we simply refer to d(MIM)/dz as the MIM signal, and the simulations were done accordingly.

Raman characterization

The collinear polarization low-frequency Raman spectroscopy was performed under normal incidence using a diode-pumped solid-state laser with an excitation wavelength of 532 nm. A linearly polarized laser beam was focused on the sample by a 40× objective to a diameter of 1 to 2 μm. The reflected radiation with polarization parallel to the inherent polarization of the excitation beam was collected by a grating spectrometer equipped with a thermoelectrically cooled charge-coupled device. The Rayleigh line was suppressed using three notch filters with an optical density of 3 and a spectral bandwidth of ~10 cm^{-1}. A typical laser power of 0.25 mW was used to avoid sample heating. The sample temperature was fixed at 5 K.

SUPPLEMENTARY MATERIALS

Supplementary material for this article is available at http://advances.sciencemag.org/cgi/content/full/5/2/eaat8799/DC1

Section S1. Sample structures
Section S2. MIM images of monolayer WTe_2 flake
Section S3. Gate dependence of transport and MIM signals
Section S4. Simulation of the edge parameters
Section S5. The monolayer/bilayer WTe_2 flake in Fig. 3
Section S6. Gate dependence of internal cracks
Fig. S1. MIM-Im images taken for a large monolayer WTe_2 flake, overlaid on the optical image at $T = 8$ K and $B = 0$.
Fig. S2. Gate-dependent MIM images of the sample presented in Fig. 4C.
Fig. S3. Gate dependence of transport and MIM.
Fig. S4. Simulation of MIM near the edge.
Fig. S5. Conceptual model of the effects of disorder on the edge conduction in a magnetic field.
Fig. S6. AFM topography image of the monolayer WTe_2 flake presented in Fig. 3 (A to D).
Fig. S7. Gate dependence of internal cracks.
Table S1. Information of the monolayer WTe_2 samples presented in the main text.

REFERENCES AND NOTES

1. C. L. Kane, E. J. Mele, Quantum spin Hall effect in graphene. *Phys. Rev. Lett.* **95**, 226801 (2005).
2. C. L. Kane, E. J. Mele, Z_2 topological order and the quantum spin Hall effect. *Phys. Rev. Lett.* **95**, 146802 (2005).
3. B. A. Bernevig, S.-C. Zhang, Quantum spin Hall effect. *Phys. Rev. Lett.* **96**, 106802 (2006).
4. X.-L. Qi, S.-C. Zhang, Topological insulators and superconductors. *Rev. Mod. Phys.* **83**, 1057–1110 (2011).
5. M. Z. Hasan, C. L. Kane, *Colloquium*: Topological insulators. *Rev. Mod. Phys.* **82**, 3045–3067 (2010).
6. X. Qian, J. Liu, L. Fu, J. Li, Quantum spin Hall effect in two-dimensional transition metal dichalcogenides. *Science* **346**, 1344–1347 (2014).
7. B. A. Bernevig, T. L. Hughes, S.-C. Zhang, Quantum spin Hall effect and topological phase transition in HgTe quantum wells. *Science* **314**, 1757–1761 (2006).
8. M. König, S. Wiedmann, C. Brüne, A. Roth, H. Buhmann, L. W. Molenkamp, X.-L. Qi, S.-C. Zhang, Quantum spin Hall insulator state in HgTe quantum wells. *Science* **318**, 766–770 (2007).
9. A. Roth, C. Brüne, H. Buhmann, L. W. Molenkamp, J. Maciejko, X.-L. Qi, S.-C. Zhang, Nonlocal transport in the quantum spin Hall state. *Science* **325**, 294–297 (2009).
10. C. Brüne, A. Roth, H. Buhmann, E. M. Hankiewicz, L. W. Molenkamp, J. Maciejko, X.-L. Qi, S.-C. Zhang, Spin polarization of the quantum spin Hall edge states. *Nat. Phys.* **8**, 486–491 (2012).
11. K. C. Nowack, E. M. Spanton, M. Baenninger, M. König, J. R. Kirtley, B. Kalisky, C. Ames, P. Leubner, C. Brüne, H. Buhmann, L. W. Molenkamp, D. Goldhaber-Gordon, K. A. Moler, Imaging currents in HgTe quantum wells in the quantum spin Hall regime. *Nat. Mater.* **12**, 787–791 (2013).
12. I. Knez, R.-R. Du, G. Sullivan, Evidence for helical edge modes in inverted InAs/GaSb quantum wells. *Phys. Rev. Lett.* **107**, 136603 (2011).
13. K. Suzuki, Y. Harada, K. Onomitsu, K. Muraki, Edge channel transport in the InAs/GaSb topological insulating phase. *Phys. Rev. B* **87**, 235311 (2013).
14. E. M. Spanton, K. C. Nowack, L. Du, G. Sullivan, R.-R. Du, K. A. Moler, Images of edge current in InAs/GaSb quantum wells. *Phys. Rev. Lett.* **113**, 026804 (2014).
15. L. Du, I. Knez, G. Sullivan, R.-R. Du, Robust helical edge transport in gated InAs/GaSb bilayers. *Phys. Rev. Lett.* **114**, 096802 (2015).
16. Z. Fei, T. Palomaki, S. Wu, W. Zhao, X. Cai, B. Sun, P. Nguyen, J. Finney, X. Xu, D. H. Cobden, Edge conduction in monolayer WTe_2. *Nat. Phys.* **13**, 677–682 (2017).
17. S. Tang, C. Zhang, D. Wong, Z. Pedramrazi, H.-Z. Tsai, C. Jia, B. Moritz, M. Claassen, H. Ryu, S. Kahn, J. Jiang, H. Yan, M. Hashimoto, D. Lu, R. G. Moore, C.-C. Hwang, C. Hwang, Z. Hussain, Y. Chen, M. M. Ugeda, Z. Liu, X. Xie, T. P. Devereaux, M. F. Crommie, S.-K. Mo, Z.-X. Shen, Quantum spin Hall state in monolayer 1T′-WTe_2. *Nat. Phys.* **13**, 683–687 (2017).
18. Z.-Y. Jia, Y.-H. Song, X.-B. Li, K. Ran, P. Lu, H.-J. Zheng, X.-Y. Zhu, Z.-Q. Shi, J. Sun, J. Wen, D. Xing, S.-C. Li, Direct visualization of a two-dimensional topological insulator in the single-layer 1T′–WTe_2. *Phys. Rev. B* **96**, 041108 (2017).
19. S. Wu, V. Fatemi, Q. D. Gibson, K. Watanabe, T. Taniguchi, R. J. Cava, P. Jarillo-Herrero, Observation of the quantum spin Hall effect up to 100 kelvin in a monolayer crystal. *Science* **359**, 76–79 (2018).
20. T. Li, P. Wang, H. Fu, L. Du, K. A. Schreiber, X. Mu, X. Liu, G. Sullivan, G. A. Csáthy, X. Lin, R.-R. Du, Observation of a helical luttinger liquid in InAs/GaSb quantum spin Hall edges. *Phys. Rev. Lett.* **115**, 136804 (2015).
21. F. Nichele, H. J. Suominen, M. Kjaergaard, C. M. Marcus, E. Sajadi, J. A. Folk, F. Qu, A. J. A. Beukman, F. K. de Vries, J. van Veen, S. Nadj-Perge, L. P. Kouwenhoven,

B.-M. Nguyen, A. A. Kiselev, W. Yi, M. Sokolich, M. J. Manfra, E. M. Spanton, K. A. Moler, Edge transport in the trivial phase of InAs/GaSb. *New J. Phys.* **18**, 083005 (2016).
22. E. Y. Ma, M. R. Calvo, J. Wang, B. Lian, M. Mühlbauer, C. Brüne, Y.-T. Cui, K. Lai, W. Kundhikanjana, Y. Yang, M. Baenninger, M. König, C. Ames, H. Buhmann, P. Leubner, L. W. Molenkamp, S.-C. Zhang, D. Goldhaber-Gordon, M. A. Kelly, Z.-X. Shen, Unexpected edge conduction in mercury telluride quantum wells under broken time-reversal symmetry. *Nat. Commun.* **6**, 7252 (2015).
23. K. Lai, M. B. Ji, N. Leindecker, M. A. Kelly, Z. X. Shen, Atomic-force-microscope-compatible near-field scanning microwave microscope with separated excitation and sensing probes. *Rev. Sci. Instrum.* **78**, 063702 (2007).
24. Y.-T. Cui, B. Wen, E. Y. Ma, G. Diankov, Z. Han, F. Amet, T. Taniguchi, K. Watanabe, D. Goldhaber-Gordon, C. R. Dean, Z.-X. Shen, Unconventional correlation between quantum Hall transport quantization and bulk state filling in gated graphene devices. *Phys. Rev. Lett.* **117**, 186601 (2016).
25. Y.-T. Cui, E. Y. Ma, Z.-X. Shen, Quartz tuning fork based microwave impedance microscopy. *Rev. Sci. Instrum.* **87**, 063711 (2016).
26. M. König, H. Buhmann, L. W. Molenkamp, T. Hughes, C.-X. Liu, X.-L. Qi, S.-C. Zhang, The quantum spin Hall effect: Theory and experiment. *J. Phys. Soc. Jpn.* **77**, 031007 (2008).
27. M. V. Bollinger, J. V. Lauritsen, K. W. Jacobsen, J. K. Nørskov, S. Helveg, F. Besenbacher, One-dimensional metallic edge states in MoS_2. *Phys. Rev. Lett.* **87**, 196803 (2001).
28. C. Zhang, A. Johnson, C.-L. Hsu, L.-J. Li, C.-K. Shih, Direct imaging of band profile in single layer MoS_2 on graphite: Quasiparticle energy gap, metallic edge states, and edge band bending. *Nano Lett.* **14**, 2443–2447 (2014).
29. D. Wu, X. Li, L. Luan, X. Wu, W. Li, M. N. Yogeesh, R. Ghosh, Z. Chu, D. Akinwande, Q. Niu, K. Lai, Uncovering edge states and electrical inhomogeneity in MoS_2 field-effect transistors. *Proc. Natl. Acad. Sci. U.S.A.* **113**, 8583–8588 (2016).
30. N. Levy, S. A. Burke, K. L. Meaker, M. Panlasigui, A. Zettl, F. Guinea, A. H. Castro Neto, M. F. Crommie, Strain-induced pseudo–magnetic fields greater than 300 tesla in graphene nanobubbles. *Science* **329**, 544–547 (2010).
31. S. Mi, D. I. Pikulin, M. Wimmer, C. W. J. Beenakker, Proposal for the detection and braiding of Majorana fermions in a quantum spin Hall insulator. *Phys. Rev. B* **87**, 241405 (2013).
32. P. J. Zomer, M. H. D. Guimarães, J. C. Brant, N. Tombros, B. J. van Wees, Fast pick up technique for high quality heterostructures of bilayer graphene and hexagonal boron nitride. *Appl. Phys. Lett.* **105**, 013101 (2014).

Acknowledgments: We thank E. Y. Ma, Z. Wei, and X. Chen for helpful discussions. **Funding:** The work at UCR was supported by the start-up funds from the Regents of the University of California. The work at UW was supported by DoE BES grants DE-SC0002197 (to D.H.C.) and DE-SC0018171 (to X.X.). Z.F. and X.C. were partially supported by NSF MRSEC 1719797. The work at Stanford University was supported by the Gordon and Betty Moore Foundation through the Emergent Phenomena in Quantum Systems (EPiQS) initiative GBMF4546 to Z.-X.S. B.N. and D.W. acknowledge financial support from the State Key Program for Basic Research of China (contract no. 2015CB921203). B.N.'s visit at UCR was supported by the China Scholarship Council (CSC). **Author contributions:** Y.-T.C., D.H.C., and X.X. conceived the experiment. Y.S., B.N., B.A.F., and Y.-T.C. performed the MIM measurements. J.K., Z.F., and B.S. fabricated the devices. X.C. performed the Raman measurements. Y.-T.C. and B.N. performed the finite element simulation. Z.-X.S. provided access to MIM measurements at He-3 temperature. D.W. provided support for B.N.'s visit to UCR. Y.-T.C., D.H.C., and X.X. analyzed the data and wrote the paper with comments from all authors. **Competing interests:** Z.-X.S. is a cofounder of PrimeNano Inc., which licensed the MIM technology from Stanford University for the commercial instrument. This technology was modified for low-temperature measurement in this report. All other authors declare that they have no competing interests. **Data and materials availability:** All data needed to evaluate the conclusions in the paper are present in the paper and/or the Supplementary Materials. Additional data related to this paper may be requested from the corresponding authors.

Submitted 13 April 2018
Accepted 21 December 2018
Published 8 February 2019
10.1126/sciadv.aat8799

Citation: Y. Shi, J. Kahn, B. Niu, Z. Fei, B. Sun, X. Cai, B. A. Francisco, D. Wu, Z.-X. Shen, X. Xu, D. H. Cobden, Y.-T. Cui, Imaging quantum spin Hall edges in monolayer WTe_2. *Sci. Adv.* **5**, eaat8799 (2019).

ScienceAdvances

Imaging quantum spin Hall edges in monolayer WTe_2

Yanmeng Shi, Joshua Kahn, Ben Niu, Zaiyao Fei, Bosong Sun, Xinghan Cai, Brian A. Francisco, Di Wu, Zhi-Xun Shen, Xiaodong Xu, David H. Cobden and Yong-Tao Cui

Sci Adv **5** (2), eaat8799.
DOI: 10.1126/sciadv.aat8799